AGU PUBLICATIONS

JGR

Journal of Geophysical Research: Space Physics

RESEARCH ARTICLE

10.1002/2014JA020560

Key Points:
- Distribution of amplitudes follows lognormal distribution with a power law tail
- Amplitudes fall off with increasing depth inside downstream foreshock
- Modulational instability is not relevant in Langmuir wave saturation at Saturn

Correspondence to:
D. Píša,
david-pisa@uiowa.edu

Citation:
Píša, D., G. B. Hospodarsky, W. S. Kurth, O. Santolík, J. Souček, D. A. Gurnett, A. Masters, and M. E. Hill (2015), Statistics of Langmuir wave amplitudes observed inside Saturn's foreshock by the Cassini spacecraft, *J. Geophys. Res. Space Physics*, *120*, 2531–2542, doi:10.1002/2014JA020560.

Received 29 AUG 2014
Accepted 23 FEB 2015
Accepted article online 1 MAR 2015
Published online 10 APR 2015

Statistics of Langmuir wave amplitudes observed inside Saturn's foreshock by the Cassini spacecraft

David Píša[1,2], George B. Hospodarsky[1], William S. Kurth[1], Ondřej Santolík[2,3], Jan Souček[2], Donald A. Gurnett[1], Adam Masters[4], and Matthew E. Hill[5]

[1]Department of Physics and Astronomy, University of Iowa, Iowa City, Iowa, USA, [2]Institute of Atmospheric Physics AS CR, Prague, Czech Republic, [3]Faculty of Mathematics and Physics, Charles University in Prague, Prague, Czech Republic, [4]Space and Atmospheric Physics Group, The Blackett Laboratory, Imperial College London, London, UK, [5]Applied Physics Laboratory, Johns Hopkins University, Laurel, Maryland, USA

Abstract We present the first systematic study of Langmuir wave amplitudes in Saturn's foreshock using the Cassini Radio and Plasma Wave Science/Wideband Receiver measurements. We analyzed all foreshock crossings from June 2004 to December 2009 using an automatic method to identify Langmuir waves. Using this method, almost 3×10^5 waveform intervals of typical duration of about a minute were selected. For each selected waveform interval the position of the satellite inside the foreshock was calculated using an adaptive bow shock model, which was parametrized by the observed magnetic field and plasma data. We determined the wave amplitudes for all waveform intervals, and we found that the probability density function amplitudes follow a lognormal distribution with a power law tail. A nonlinear fit for this tail gives a power law exponent of -1.37 ± 0.01. The distribution of amplitudes as a function of the depth in the foreshock shows the onset of the waves near the upstream boundary with its maximum slightly shifted inside the foreshock ($\sim 1\ R_S$). The amplitudes then fall off with increasing depth in the downstream region. Our results are in agreement with previous observations and roughly follow the generally accepted stochastic growth theory mechanism for the foreshock region, with an exception at the highest observed amplitudes. The estimated energy density ratio W for largest amplitudes does not exceed 10^{-2}, suggesting that modulational instability is not relevant for a large majority of waves. The decay instability can be important for the stronger electrostatic waves in Saturn's foreshock, as was previously reported for multiple solar system planets.

1. Introduction

In front of planetary magnetospheres the solar wind flow forms a collisionless bow shock. The bow shock and its tangent interplanetary magnetic field line delimit boundaries of the region called the foreshock [*Greenstadt*, 1976]. The foreshock is the upstream region magnetically connected to the planetary bow shock. It is composed of the convecting solar wind plasma and energetic particles reflected from the bow shock. The region closer to the tangent field line is filled by streaming electrons, and it is often called the electron foreshock. The region further downstream is filled with streaming ions and electrons and is often called the ion foreshock. More detailed descriptions of the upstream and downstream region of planetary bow shocks can be found in *Tsurutani and Stone* [1985]. The reflected electrons create beams, which can, due to the time-of-flight effect, result in a bump-on-tail distribution function. This electron distribution function is unstable and gives arise to the beam-plasma instability generating electrostatic Langmuir waves at frequencies close to the local plasma frequency [e.g., *Scarf et al.*, 1971].

Earlier studies reported the observation of Langmuir waves in the planetary foreshocks of Venus, Earth, Jupiter, Saturn, Uranus, and Neptune [*Anderson et al.*, 1981; *Gurnett et al.*, 1981, 1986, 1992; *Hospodarsky et al.*, 1994; *Boshuizen et al.*, 2004, and references therein]. In most of these studies spectral density measurements were obtained by receivers with integration times longer than the typical Langmuir wave packets. This fact could lead to the underestimation of wave amplitudes due to temporal and spatial averaging. Recently, more detailed studies of Langmuir waves in the terrestrial foreshock were done using waveforms captured by Wind [*Bale et al.*, 1997a], Cluster [*Sigsbee et al.*, 2004a, 2004b; *Soucek et al.*, 2005; *Krasnoselskikh et al.*, 2007; *Musatenko et al.*, 2007], and STEREO spacecraft [*Malaspina et al.*, 2009].

Langmuir waves are often observed close to the upstream foreshock boundary as a long burst of narrow band emissions. However, deeper inside the foreshock and close to the magnetosheath, Langmuir waves are nonstationary and can spread in a wide frequency range showing upshifted and downshifted electrostatic waves [e.g., *Etcheto and Faucheux*, 1984]. At Earth, the maximum wave intensity was observed near the upstream foreshock boundary with a slight shift behind the tangent field line toward the downstream position (depth) and with a relatively slow decrease deeper in the foreshock [*Cairns et al.*, 1997; *Sigsbee et al.*, 2004b]. The wave amplitude also decreases with distance along the tangent field line but much slower compared to the dependence on the depth [e.g., *Etcheto and Faucheux*, 1984; *Malaspina et al.*, 2009].

The stochastic growth theory (SGT) [e.g., *Robinson*, 1992; *Robinson and Cairns*, 1993; *Robinson*, 1995; *Cairns and Robinson*, 1997] gives an explanation for the probability distribution function of wave amplitudes. SGT suggests that the interaction of an electron beam with a plasma is close to a state of marginal stability with a growth rate varying stochastically. If nonlinear and thermal effects are neglected, the distribution of wave amplitudes should follow a lognormal distribution [*Robinson*, 1995]. Event studies using experimental data observed during a time period of hours and covering only spatially limited regions found the distribution of amplitudes close to lognormal across most foreshock regions [e.g., *Cairns et al.*, 1997; *Sigsbee et al.*, 2004a]. However, observations mixing a wide range of foreshock positions show amplitude distributions following a power law distribution at high amplitudes with an exponent ≈ -1 [*Bale et al.*, 1997b; *Cairns et al.*, 1997; *Boshuizen et al.*, 2004]. This can be explained by an aggregated amplitude distribution, as a result of a combination of many lognormal distributions for spatially limited regions [*Boshuizen et al.*, 2001].

This study presents the first statistical analysis of Langmuir wave amplitudes using electric field waveform measurements obtained by the Radio and Plasma Wave Science (RPWS) Wideband Receiver on board the Cassini spacecraft over almost 6 years of its mission at Saturn. Typical conditions in the solar wind at Saturn orbit are different to those at the Earth. The strength of the interplanetary magnetic field (IMF) and solar wind density are ~1 and ~2 orders of magnitude lower, respectively, and the typical Parker spiral angle increases from ~45° to ~86° [*Jackman et al.*, 2008]. The configuration of the Saturnian bow shock and the direction of the IMF allows Cassini to observe Langmuir waves in both dawn (06–12 h) and dusk (12–18 h) magnetic local time (MLT) sectors (shown as the gray region in Figure 1), which are in case of Saturn identical with local time sectors. We follow generally accepted convention for similar region at other planets in the solar system and call this region the foreshock. During the mission, Cassini crossed almost all possible MLT sectors where Langmuir waves could be observed. We present the first comprehensive statistics of foreshock Langmuir waves at Saturn based on detailed waveform measurements. Although Langmuir waves dominate in the electron foreshock, they can be also observed inside the ion foreshock [*Fuselier et al.*, 1985], so we do not distinguish between the electron and ion foreshock in this study. Section 2 is devoted to a brief description of the instrumentation. Methods of analysis are explained in section 3, and section 4 summarizes the results. Conclusions are given in section 5.

2. Instrumentation

For the purpose of this study we used data from the Radio and Plasma Wave Science (RPWS) and the Magnetometer (MAG) instruments on board the Cassini spacecraft. The RPWS instrument consists of three electric antennas, a Langmuir probe, a triaxial search coil magnetometer, and five specialized receivers. The receivers cover a range from ~1 Hz to 16 MHz for the electric fields and ~1 Hz to 12 kHz for the magnetic fields. The frequency range of the Langmuir waves detected at Saturn falls into the frequency interval recorded by the Wideband Receiver (WBR). The WBR provides waveform measurements over a bandwidth of either 60 Hz to 10.5 kHz (10 kHz mode) or 800 Hz to 75 kHz (80 kHz mode). We used the 10 kHz Wideband waveform intervals with a sampling frequency of 27.7 kHz and with a typical duration of ~37 or ~74 ms (1024 or 2048 samples) captured every 125 ms. The typical duration of the 10 kHz Wideband capture mode is usually about 1.5 min. Due to limitations on spacecraft telemetry, this mode is not continuous. Only several time intervals per 1 h are typically available. Most of the time, the signal from the dipole antenna (effective length of 9.26 m) parallel to the spacecraft x axis is processed. The total dynamic range of the receiver is 118 dB, thanks to a set of a discrete gain amplifiers and an automatic gain control. This corresponds to the amplitude range from 2.33×10^{-4} to 1.85×10^{2} mV/m. The automatic gain control amplifies the signal in steps of 10 dB over the range of 0–70 dB with a time constant of ~0.1 s. While the WBR typically

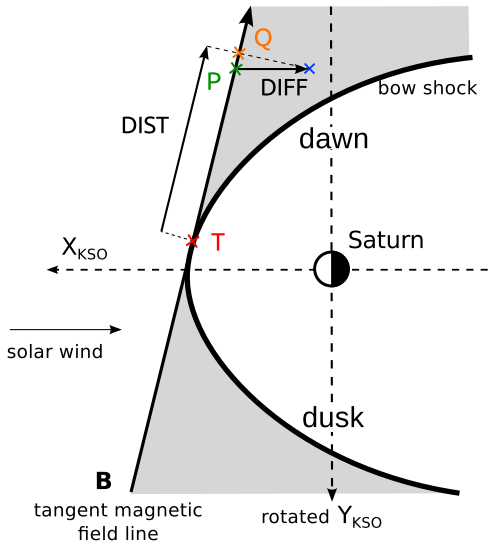

Figure 1. Schematic illustration of the foreshock coordinate system in the rotated KSO coordinate system. The red cross shows the position of the tangent point T for a bow shock and a magnetic field line. The satellite's position is shown by the blue cross, downstream along the solar wind velocity from the point P on the tangent line. Point Q shows the closest point on the tangent line to the satellite position. The shaded region delimits the foreshock regions.

obtains a waveform every 125 ms, the gain time constant causes the update to be made for a subsequent waveform capture. Therefore, waveforms with rapidly changing amplitudes can be digitally clipped. For a more detailed description of the instrument and modes of operation, see *Gurnett et al.* [2004].

The MAG instrument consists of two independent magnetometers. The first one is a vector/scalar helium magnetometer providing the vector field up to ±256 nT or the field magnitude in a range 256 to 16,385 nT. The second magnetometer, the fluxgate magnetometer, uses triaxial fluxgate sensors and operates in one of four ranges up to ±44,000 nT. We used the fluxgate magnetometer data with a time resolution of 1 s. The full description of the instrument has been given by *Dougherty et al.* [2004].

3. Methods of Analysis

In the first step of the analysis all positions of the Cassini spacecraft outside of the bow shock have been selected. We have used a list of bow shock crossings visually identified from the magnetometer and the plasma spectrometer data (http://mapsview.engin.umich.edu). The bow shock crossings are identified by sharp changes of the magnetic field amplitude and the plasma density and temperature. The strength and variability of magnetic field is higher in downstream of the bow shock. Inside the magnetosheath a hotter and denser electron population is observed, whereas upstream of the bow shock the cooler solar wind electron distribution is measured [see *Masters et al.*, 2008, Figure 2]. The projections of Cassini's orbits onto the Kronocentric Solar Orbital (KSO) equatorial and meridional planes between June 2004 and December 2009 with distances up to 70 R_S (where R_S is the Saturn's radius) are shown in Figure 2. Positions inside and outside of the bow shock are shown in blue and red colors, respectively. All 10 kHz Wideband data outside of the bow shock were analyzed. Intervals with clipped waveform were excluded. The remaining waveform intervals were calibrated, and their power spectra were calculated. Langmuir waves detected at Saturn typically fall into the frequency interval from 1.5 to 10 kHz [*Scarf et al.*, 1982]. Therefore, an automated procedure looked for spectral peaks of wave power within a frequency range between 1.5 and 10 kHz. The lower frequency limit is also used to exclude spacecraft noise and interference occurring below 1.5 kHz, especially during the later part of the mission (after 2007). Figure 3a shows an example of a waveform interval containing Langmuir wave emissions and an intense low-frequency component (~50 Hz). The same waveform after using a digital high-pass filter of tenth order with a cutoff frequency $f_c = 1.5$ kHz is shown in Figure 3b. The automated procedure identifies the maximum peak in each spectrum and estimates a background noise level using a derivative of the spectrum. The background noise level is calculated as a mean value of the minimum on both sides of the peak. Spectra where the peak intensity is at least 10 dB above the background noise level for the given waveform interval were selected. Langmuir waves are one of the most powerful emissions in their frequency range in the region outside of the bow shock; therefore, they can usually be easily distinguished from the background noise. Almost 3×10^5 waveform intervals of the 10 kHz wideband mode with Langmuir waves signatures were identified. For all selected intervals, time-frequency spectrograms were plotted and visually checked for possible bad identifications.

Subsequently, each selected waveform interval was multiplied by a correction factor for the antenna orientation with respect to the ambient magnetic field [*Gurnett and Bhattacharjee*, 2005]. The direction of the electric field vector of Langmuir waves is always very close to the direction of the magnetic field. The

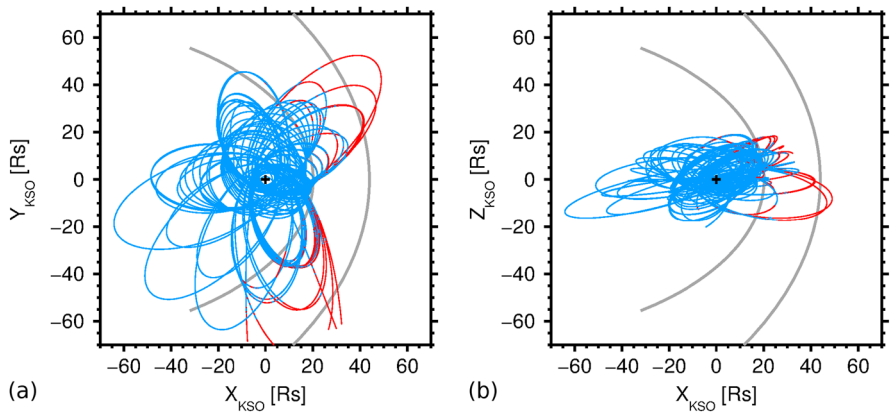

Figure 2. Projections of Cassini's positions projected onto the (a) *X-Y* and (b) *X-Z* plane in the Kronocentric Solar Orbital (KSO) coordinate system (in Saturn's radii, R_S) for the time period between June 2004 and December 2009 and for radial distances less than 70 R_S. Gray lines show two intersections of Saturn's bow shock with the same plane for two values of the solar wind dynamic pressure: for $p_{dyn} = 0.003$ nPa (more distant from the planet) and for $p_{dyn} = 0.2$ nPa (closer to the planet) obtained from the model of *Went et al.* [2011]. Positions inside and outside of the bow shock are plotted in blue and red colors, respectively. Note that positions with high z_{KSO} labeled as outside of the shock (red color) can be projected on the X-Y_{KSO} plane inside its intersection with the shock model (gray line). The position of Saturn is shown by the black cross at the origin of the KSO coordinate system.

orientation of the receiving antenna with respect to the direction of the magnetic field therefore influences the measured wave amplitudes. A correction factor of $1/\cos\theta$, where θ is the angle between the dipole antenna and the magnetic field, was applied for each received waveform interval [*Sigsbee et al.*, 2004a]. When the angle between the antenna and the magnetic field is close to 90° ($78° > \theta > 101°$), the correction factor becomes large and uncertainties of the measurements increase. These observations were therefore also excluded from the analysis. All criteria were met by more than 2×10^5 waveform intervals.

To organize our results, an estimation of the satellite's position with respect to the foreshock boundary was made. The direction of the magnetic field from the Cassini MAG instrument at 1 s time resolution and a semiempirical adaptive model of the Saturn's bow shock of *Went et al.* [2011] were used. For this model the solar wind dynamic pressure was calculated using the solar wind speed obtained from measurements of the Cassini MIMI instrument (http://mapsview.engin.umich.edu). These data are available up to January 2005. For later years, the averaged speed estimated from the first 7 months (June 2004 to January 2005) of Cassini's Saturn mission was used ($v_{sw} = 445$ km/s). The upstream solar wind electron density was calculated from the frequency of the detected Langmuir waves. Estimates of bow shock positions for two values of the solar wind dynamic pressure ($p_{dyn} = 0.003$ and 0.2 nPa) from Went's model are shown by gray lines in Figure 2.

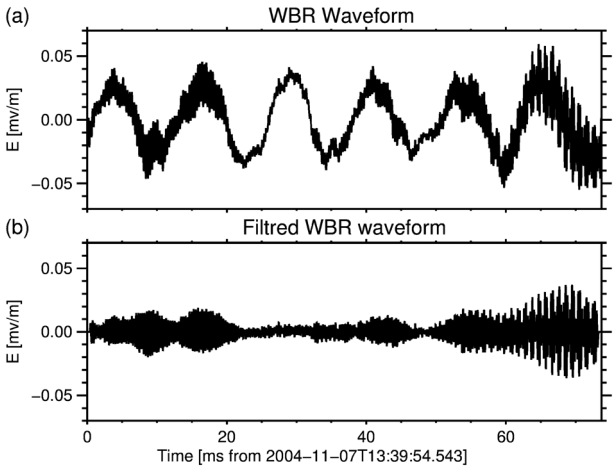

Figure 3. An example of the WBR electric field waveform with Langmuir wave emission observed on 7 November 2004. (a) A measured waveform interval modulated by an intense low-frequency component. (b) The same waveform interval after applying a digital high-pass filter of tenth order with a cutoff frequency $f_c = 1.5$ kHz.

For each waveform interval in our data set, we calculated foreshock coordinates using the method and terminology which was introduced by *Filbert and Kellogg* [1979] and later modified by *Cairns and Robinson* [1997]. First, a tangent line to the bow shock model, drawn along the magnetic field direction is defined so that the spacecraft position can be shifted along the solar wind

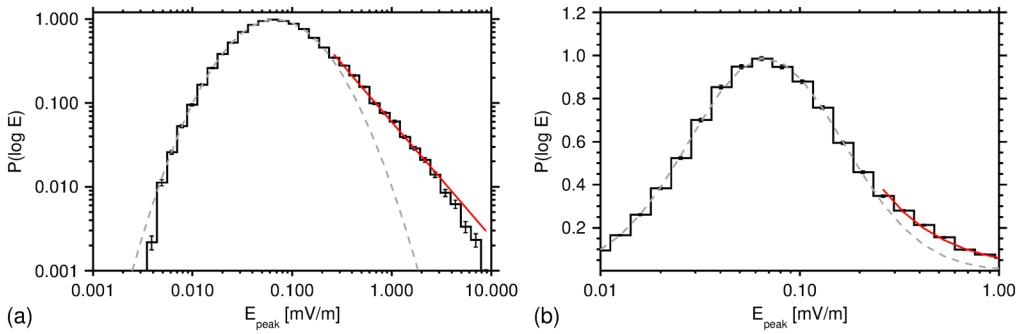

Figure 4. Probability distribution of wave amplitudes for the electric field of selected waveform intervals observed by the Cassini WBR. The gray dashed line represents a fit of a lognormal distribution with parameters $\langle \log E \rangle = -1.170 \pm 0.002$, $\sigma_{\log E} = 0.387 \pm 0.001$. The red line shows the high amplitude fit (from 0.25 to 10 mV/m) with a power law exponent of $= -1.37 \pm 0.01$. (a) Overall amplitude distribution using a log scale. (b) Detail of distribution function for amplitudes between 0.01 and 0.1 mV/m using a linear scale.

direction to a point P on the tangent line. The DIFF (also known as (aka) D_f) coordinate is then measured along the solar wind direction (assumed to be parallel with the $\hat{x}_{KSO}$ axis) positive in the downstream direction from point P on the tangent line to the spacecraft position (see Figure 1). The DIST (aka R) coordinate is defined as a distance between point T, where the tangent line touches the bow shock, and point Q, which lies on the tangent line closest to the satellite position. Observations for which the absolute value of the angle between the magnetic field and the direction of the solar wind was lower than 45° were excluded. Smaller angles place the tangent point deep behind the nose of the bow shock, and an unrealistic foreshock position would be obtained. More than $\sim 1.7 \times 10^5$ waveform intervals remained after this step of the analysis procedure.

4. Distribution of Amplitudes

Langmuir waves were systematically observed within Saturn's foreshock during the approach to Saturn after 7 June 2004, from distances of ~220 R_S. After the Saturn orbit insertion on 1 July 2004, Cassini was rarely further than 70 R_S from Saturn. Our analysis is limited to distances up to 100 R_S in both foreshock coordinates.

From each processed waveform interval (~37 or ~74 ms), the maximum electric field amplitude was obtained. To estimate the amplitude probability density function, the full 118 dB WBR range was divided into 2 dB wide bins. The obtained probability distribution for the amplitudes of the observed Langmuir waves is shown in Figure 4. Bins are equidistantly distributed on the logarithmic scale. The dashed gray line shows the fit of the lognormal distribution with mean value $\langle \log E \rangle = -1.129 \pm 0.001$, standard deviation $\sigma_{\log E} = 0.396 \pm 0.001$ for amplitudes from 0.005 to 0.25 mV/m. A nonlinear least squares fit with a Poisson standard deviation of each point has been used [*Press et al.*, 1992]. One can see deviations of the amplitude distribution from the lognormal law for amplitudes >0.25 mV/m. The amplitude distribution for amplitudes <0.005 mV/m is affected by the threshold for the automated procedure. Higher amplitudes from 0.25 to 10 mV/m were therefore fitted by a power law distribution with an exponent of -1.37 ± 0.01. The possible influence of data selection on the amplitude distribution related to the antenna correction and the foreshock position is discussed in section 5.

The probability distribution of wave amplitudes observed within two spatially limited regions is shown in Figure 5. We have selected two distinct region, close to the upstream boundary and deeper inside the foreshock with similar number of observations. The black line represents amplitudes observed in the region with DIFF between 0 and 10 R_S and DIST <20 R_S. The gray line shows amplitude distribution from the region with DIFF between 20 and 25 R_S and DIST >55 R_S. Blue and red dashed lines represent a fit of a lognormal distribution with parameters $\langle \log E \rangle = -0.571 \pm 0.007$, $\sigma_{\log E} = 0.537 \pm 0.006$ and $\langle \log E \rangle = -1.221 \pm 0.004$, $\sigma_{\log E} = 0.325 \pm 0.003$, respectively. An overall interval of amplitudes with a logarithmic scale is plotted in Figure 5a, and a detail of the distribution function for amplitudes between 0.01 and 10 mV/m using a linear scale is plotted in Figure 5b. The amplitude distribution observed closer to the tangent point (black

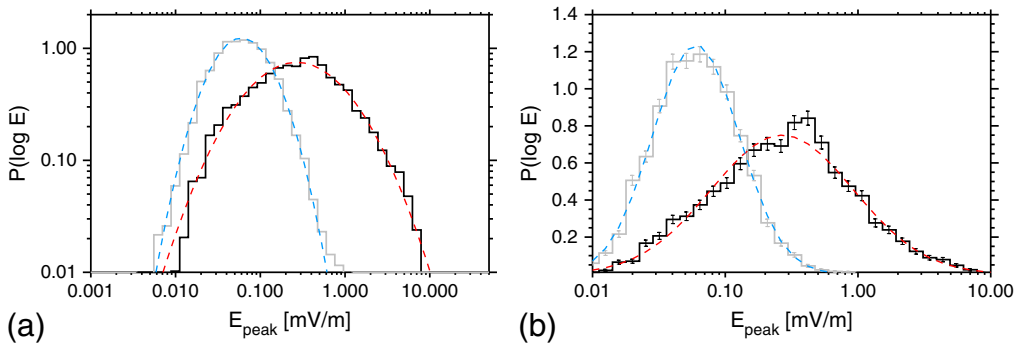

Figure 5. Probability distribution of wave amplitudes observed within spatially limited regions. The black line represents amplitudes observed in a region with DIFF between 0 and 10 R_S and DIST <20 R_S. The gray line shows amplitude distribution from a region with DIFF between 20 and 25 R_S and DIST >55 R_S. Blue and red dashed lines represent a fit of a lognormal distribution with parameters $\langle \log E \rangle = -1.571 \pm 0.007$, $\sigma_{\log E} = 0.537 \pm 0.006$ and $\langle \log E \rangle = -1.221 \pm 0.004$, $\sigma_{\log E} = 0.325 \pm 0.003$, respectively. (a) Overall amplitude scale using a log scale. (b) Detail of distribution function for amplitudes between 0.01 and 10 mV/m using a linear scale.

line) exhibits a wider distribution with the median value of 0.27 mV/m. The amplitude distribution for the region placed further from the tangent point exhibits narrower distribution with a lower median value of 0.06 mV/m. The amplitude distribution for both regions follows the lognormal distribution without a power law tail.

To take into account of the possible influence of inaccurate estimated foreshock positions due to using an averaged solar wind speed after January 2005, two data subsets, before and after January 2005, have been created. Figures 6a and 6c show the number of waveform intervals in equidistant bins of the depth (DIFF) and the logarithm of the wave amplitude inside the foreshock up to 100 R_S. The black line represents the median of the amplitude distribution in each DIFF bin with a step of 1 R_S for positions with more than

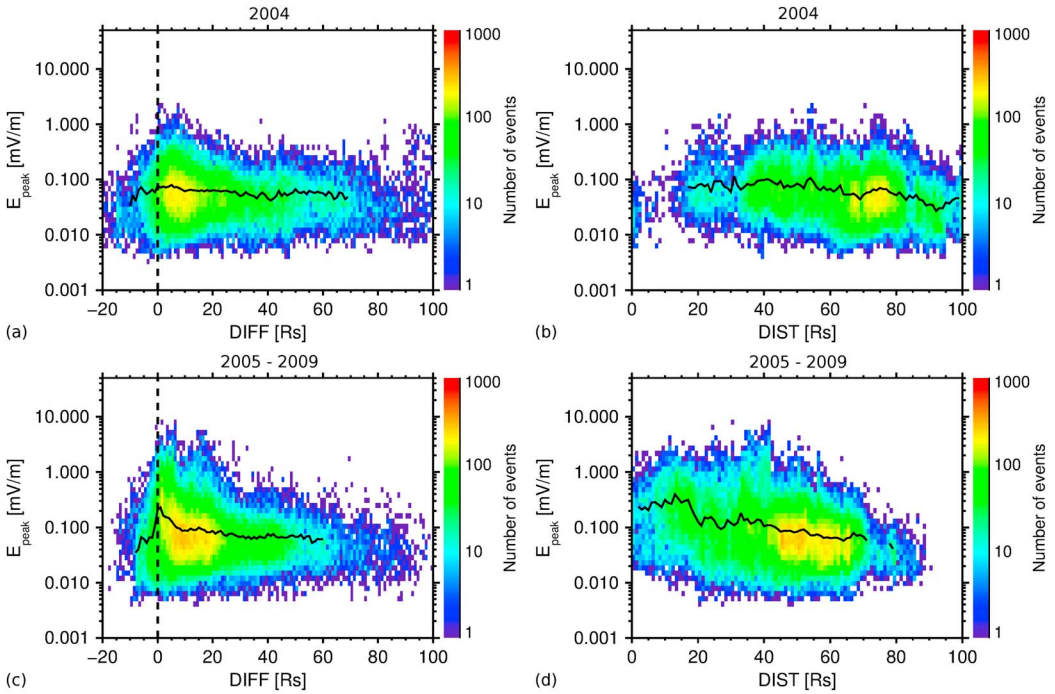

Figure 6. Number of waveform intervals in equidistant bins 0.1 log(mV/m) × 1 R_S as a function of the logarithm of the wave amplitude and (a, c) the depth (DIFF) inside the foreshock and (b, d) the distance from the tangent point along the magnetic field tangent line (DIST). The vertical dashed black line shows the upstream boundary of the bow shock (DIFF = 0). Median of the wave amplitude over foreshock coordinates is plotted by the black line with a 1 R_S step for positions with more than 100 points.

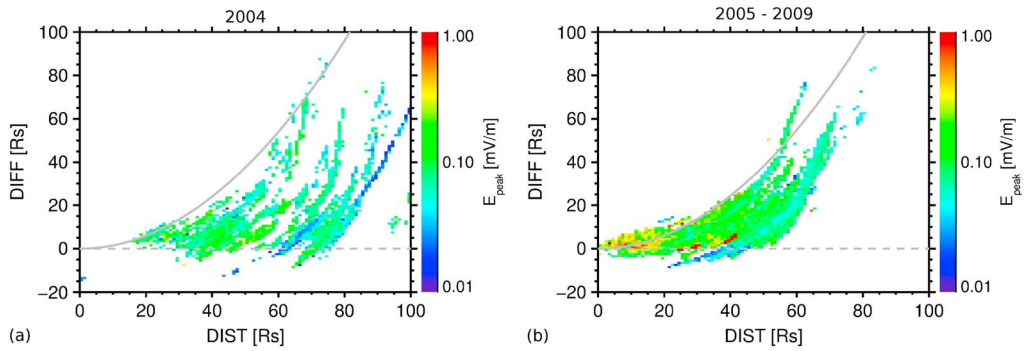

Figure 7. Median of wave amplitudes as a function of the foreshock position observed (a) before and (b) after January 2005. The tangent field line (DIFF = 0) is shown by the dashed gray line. The solid gray line represents the projection of the bow shock model for a dynamic pressure of p_{dyn} = 0.2 nPa (the closest bow shock position from the model) and a perpendicular orientation of the magnetic field with respect to the direction of the solar wind.

100 points. The dashed black line shows the position of the foreshock upstream boundary (DIFF = 0). The amplitude rises slightly with increasing DIFF from DIFF <0 and then remains constant around an amplitude of ~0.06 mV/m for the rest of the DIFF interval for observations before January 2005 shown in Figure 6a. For the time period after January 2005 plotted in Figure 6c, the amplitude increases from DIFF <0 with a maximum median amplitude ~0.23 mV/m close to the upstream foreshock boundary (DIFF = 0) at the position of DIFF = 1 R_S. With increasing depth the median amplitude decreases up to the distance of ~60 R_S. For DIFF~60 R_S, the median fluctuates around ~0.06 mV/m. Amplitude variations are largest close to the upstream foreshock boundary (DIFF = 0), and they decrease with increasing DIFF for both time periods.

The number of waveform intervals in bins as a function of the distance along the magnetic field line (DIST) up to 100 R_S and the logarithm of the wave amplitude is shown in Figures 6b and 6d. The median value of the amplitude distribution over each DIST bin with more than 100 points is plotted again by a black line. For the time period before January 2005 shown in Figure 6b, the median amplitude remains almost constant and fluctuates around ~0.08 mV/m for the DIST interval 20–60 R_S. For DIST >60 R_S, the median decreases with a minimum median amplitude ~0.03 mV/m at DIST ~90 R_S. For time period after January 2005 plotted in Figure 6d, the maximum median amplitude (~0.40 mV/m) is found at small DIST (~13 R_S). The median amplitudes decrease with the increasing distance from the tangent point. At DIST ~80 R_S, the median amplitude is lower by 1 order of magnitude (~0.04 mV/m). Amplitude variations are constant for the whole interval of DIST.

Figure 7 presents the dependence of the median amplitude on the position inside the foreshock up to 100 R_S for time period (a) before and (b) after January 2005. The dashed gray line shows the upstream foreshock boundary (DIFF = 0). The position of the model bow shock for p_{dyn} = 0.2 nPa and the tangent line for the magnetic field perpendicular to the solar wind direction are plotted by the solid gray line. Note that we use the measured magnetic field with an assumption of a straight magnetic field line between the tangent point and the point of observation. Some of the observations are therefore found outside of the idealized model foreshock boundaries in Figure 7. However, positions of the observed Langmuir waves roughly follow the expected shape of the foreshock region with the tangent magnetic field line and the bow shock as its boundaries. The median wave amplitude tends to be higher for positions close to the tangent point of the magnetic field line with the bow shock. For distant positions (DIST >55 R_S) single orbits passing through the foreshock can be identified in Figure 7.

5. Discussion

During our analysis, we have discarded a part of the data set for which a reliable correction for the electric antenna orientation was not possible. Additionally, we have rejected waveform intervals which were clipped or for which we were unable to determine their position in the foreshock accurately. The possible effect of these procedures on the distribution function of the amplitudes needs to be determined. Figure 8a shows a histogram of the number of waveforms obtained in each receiver gain state. The solid black line shows the distribution for all selected waveforms. The number of rejected waveforms due to clipping is presented by the dashed black line. The relative number of clipped waveforms is shown in the gray color part of the figure.

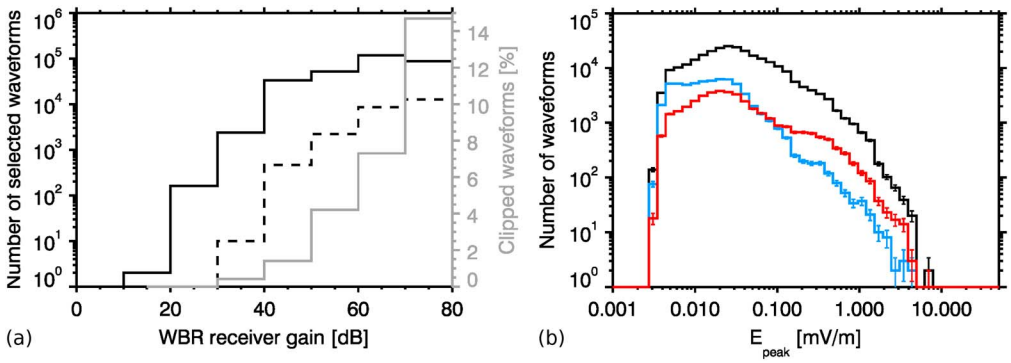

Figure 8. (a) Number of waveform intervals in each gain state of the WBR. The solid black line shows the total number of waveforms. The dashed black line represents the number of clipped waveforms. The gray line indicates the percentage of clipped waveform intervals for each gain level. (b) Number of unclipped waveform intervals selected by the automatic algorithm for the Langmuir wave detection as a function of the wave amplitude is plotted by the black line. Colored lines represent the number of waveform intervals rejected due to an inappropriate antenna correction (blue line) and an unknown and poorly determined foreshock position (red line) as a function of the wave amplitude. Data points are shown with $\pm\sqrt{N}$ error bars.

One can see that there are few rejected waveforms for lower gain states and that 14% of the waveforms were rejected at the maximum gain. This shows that higher amplitudes are less affected by the digital saturation (clipping) in the WBR receiver, but only for sudden and large intervals of wave amplitudes because the clipping mostly occurs for the higher gain states. During the later part of the mission (after 2005) the receiver gain state was rarely set to a higher gain because of growing interference from the reaction wheels used to control the attitude of the spacecraft. During this time period the minimum amplitude which was selected by the automatic algorithm increased from ~0.003 mV/m for earlier years of the mission (2004–2005) to ~0.01 mV/m for observations after 2007. In total, ~8% of preselected waveform intervals were rejected due to the clipping for all gain states.

Figure 8b shows the number of unclipped waveform intervals (black line) and rejected waveform intervals due to the unknown foreshock position (red line) and the unreliable antenna correction coefficient (blue line). The distribution of the rejected waveform intervals due to the unknown position roughly follows the distribution of unclipped waveform intervals. It shows that rejection is nearly uniformly distributed across amplitudes and there is no clear preference for certain amplitudes. Almost 14% of unclipped waveform intervals were rejected due to the unknown foreshock position. The number of rejected waveforms due to the unreliable antenna correction is higher for lower amplitudes but it follows the distribution of unclipped waveform intervals at higher amplitudes. This can be explained by lower measured amplitudes for higher angles between antenna and magnetic field. About 23% of unclipped waveform intervals were rejected due to the unreliable antenna correction. Overall, more than 52% of the waveform intervals selected by the automatic algorithm were used in the final analysis. The probability distribution of lower amplitudes (<0.004 mV/m) could be affected by a systematic rejection of smaller amplitudes due to the selection condition for the spectral peak intensity (≥10 dB) and the unreliable antenna correction. However, Figure 4 shows that lower amplitudes are in good agreement with the predicted distribution. The distribution of rejected waveforms (blue and red lines in Figure 8) for higher amplitudes (>0.04 mV/m) follows the distribution of unclipped waveform intervals. This shows that there are no preferable amplitudes for rejected waveform intervals. Therefore, the presented amplitude distribution should not be strongly affected by data selection processes during our analysis.

Typical Langmuir wave amplitudes were observed in the range of 0.01–1 mV/m with the median wave amplitude of 0.08 mV/m. The largest amplitudes have magnitudes up to ~10 mV/m. This is in agreement with previous observations inside of Saturn's foreshock from Voyager 1 [*Boshuizen et al.*, 2004] and Cassini [*Hospodarsky et al.*, 2006]. Nevertheless, the largest observed amplitudes are lower by 1 order of magnitude than wave amplitudes observed inside Earth's foreshock [e.g., *Bale et al.*, 2000; *Sigsbee et al.*, 2004a; *Malaspina et al.*, 2009]. The Langmuir wave amplitude distribution in a substantial part of the amplitude range follows the lognormal distribution ($\langle \log E \rangle = -1.170 \pm 0.002$, $\sigma_{\log E} = 0.387 \pm 0.001$) as is predicted by the stochastic growth theory [e.g., *Robinson*, 1995] and shown by several observations of Earth's

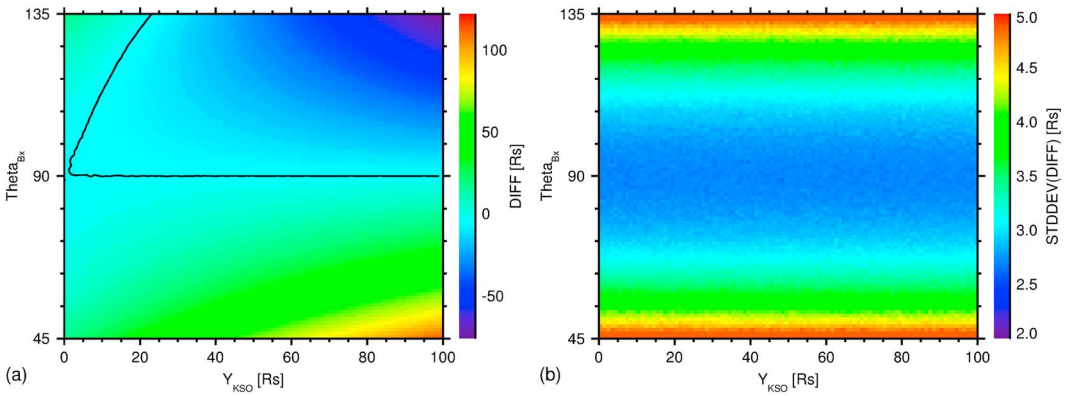

Figure 9. Results of experimentally calculated foreshock positions using the Monte Carlo method. (a) Distribution of calculated DIFF coordinates for constant $X_{KSO} = 27$ R_S as a function of Y_{KSO} positions and angles between magnetic field and solar wind direction, $Theta_{Bx}$. The black line shows the mean position on the tangent field line, DIFF = 0 R_S. (b) Distribution of the experimental uncertainties for the DIFF coordinate.

foreshock [e.g., *Cairns and Robinson*, 1997; *Sigsbee et al.*, 2004b]. However, the amplitude distribution inside Earth's foreshock was also found to follow the Pearson IV distribution [*Krasnoselskikh et al.*, 2007; *Musatenko et al.*, 2007].

We find that larger amplitudes follow a power law distribution with the exponent -1.37 ± 0.01. The power law deviations of the amplitude distribution from the lognormal law was also shown for higher amplitudes by previous observations of planetary foreshocks [e.g., *Bale et al.*, 1997a; *Sigsbee et al.*, 2004a; *Boshuizen et al.*, 2004] and can be explained by observations of the probability distribution function over wide range of foreshock positions and during different conditions in the solar wind [*Boshuizen et al.*, 2001]. Distribution of wave amplitudes observed within spatially limited region in the foreshock follows a lognormal distribution. Previous analysis of the Saturn's foreshock from the Voyager 1 measurements [*Boshuizen et al.*, 2004] shows the distribution function with a power law dependence with the exponent -0.99 ± 0.1 for combined inbound and outbound orbits. The difference from our results is probably linked to the fact that the study of *Boshuizen et al.* [2004] used data from only two Voyager 1 passes through Saturn's foreshock, while our analysis is based on a large amount of data across both dawn and dusk foreshock regions.

The wave amplitude as a function of the depth in the foreshock has a maximum close to the upstream boundary of the foreshock and decreases with depth into the downstream region. The maximum amplitude is observed to be shifted slightly (DIFF$\sim$1 R_S) deeper into the foreshock. However, our estimates of the experimental uncertainty using the Monte Carlo method show that this shift is not statistically significant. Using uncertainties in values of the bow shock parameters ($c_1 = 15 \pm 1$, $c_2 = 5.4 \pm 0.5$, and $\epsilon = 0.84 \pm 0.06$) obtained from *Went et al.* [2011], the solar wind speed from the MAPSview site ($v_{sw} = 445 \pm 54$ km/s) and constant plasma density ($n = 0.128$ cm^{-3}), the expected experimental error on the calculated DIFF coordinate for a constant $X_{KSO} = 27$ R_S as a function of the Y_{KSO} position and angle between a magnetic field and solar wind direction, $Theta_{Bx}$ is shown in Figure 9. For each position and $Theta_{Bx}$, ten thousands of foreshock coordinates were generated using parameters with normally distributed uncertainties. A distribution of mean DIFF positions is presented Figure 9a. The black line shows the mean position on the tangent field line, DIFF = 0 R_S. Figure 9b represents a standard deviation of the DIFF coordinate. One can see that the uncertainty of foreshock depth varies up to $\sim$5 R_S, depending on the distance from the tangent point and angle between the magnetic field and the solar wind direction.

Our results are in agreement with previously reported observations from Earth's foreshock. The result also shows that the model of the bow shock is generally reliable for our analysis. Visually, the upper bound of the DIFF uncertainty ($\sim$5 R_S) can be seen in Figure 7, where observed points are outside of the expected region.

Although the theory predicts that the Langmuir waves should occur only for DIFF > 0, some of our observations show their occurrence upstream of the foreshock, i.e., in front of the predicted position of the tangent field line. This inconsistency is probably related to errors in the estimation of the bow shock position and the direction of the magnetic field. The solar wind magnetic field can also be turbulent, and for that case the spacecraft can be magnetically linked with the bow shock even for positions in front of

the nominal foreshock boundary calculated from the straight-line magnetic field model. The simulation for the terrestrial foreshock shows that the turbulence can spread the boundary up to 1 R_E from the expected position [*Zimbardo and Veltri*, 1996].

The possible nonlinear mechanisms for the Langmuir wave saturation in planetary foreshocks are still under debate. Regimes of nonlinear processes inside Earth's foreshock involving turbulence, modulational instabilities as well as decay processes were discussed by many authors [e.g., *Cairns and Robinson*, 1997; *Cairns et al.*, 1998; *Bale et al.*, 2000; *Sigsbee et al.*, 2010]. To characterize the strength of the nonlinear interaction of the Langmuir waves and the plasma observed inside Saturn's foreshock, the ratio of the dimensionless energy density W is estimated. It is defined as

$$W = \frac{\epsilon_0 E^2_{\text{peak}}}{4 n_e k_b T_e} \tag{1}$$

where E_{peak} is the local peak of the electric field and n_e and T_e are the local electron density and temperature of the solar wind plasma, respectively. Using typical solar wind electron density at Saturn, $n_e = 0.11$ cm^{-3}, calculated from the mean frequency of the detected Langmuir waves ($f = 3$ kHz), the electron temperature, $T_e = 23,200$ K determined by the CAPS instrument [*Achilleos et al.*, 2006], and the upper and lower values of the peak amplitude (1×10^{-2} mV/m and 10 mV/m) gives an energy density ratio W of the range 6×10^{-9} to 6×10^{-3}. These values are consistent with the previously observed density value of 5×10^{-5} estimated from the first Cassini's approach to Saturn [*Hospodarsky et al.*, 2006] and comparable with the typical values of W observed in Earth's foreshock [e.g., *Bale et al.*, 1997a]. This result indicates that nonlinear processes, such as the electrostatic wave decay or modulational instability, are not significantly more important in the foreshock of Saturn than in the terrestrial foreshock. Since W does not exceed 10^{-2}, the arguments of *Cairns et al.* [1998] can be considered valid for Saturn's foreshock, suggesting that modulational instability is not relevant for a large majority of waves, while the decay instability can be important for the stronger electrostatic waves in this region. *Robinson and Cairns* [1995] previously arrived at a similar conclusion for multiple solar system planets based on ISEE-1, ISEE-2, and Voyager data.

6. Conclusions

We have presented the first large study of Langmuir wave amplitudes in Saturn's foreshock. We use waveform measurements from the Cassini RPWS/WBR. Data were obtained from all waveform intervals measured inside Saturn's foreshock using the 10 kHz WBR mode in years 2004–2009. An algorithm for the automatic detection of Langmuir waves was used, and almost 3×10^5 waveform intervals were selected. All selected waveform intervals were processed, and biases caused by low-frequency interference and antenna orientation were corrected. Typical Langmuir wave electric field intensities in Saturn's foreshock were observed in the range of 0.01–1 mV/m with the median wave amplitude of 0.08 mV/m. Amplitudes greater than 10 mV/m were rarely observed. The Langmuir wave amplitude distribution for most of the amplitude interval follows a lognormal law as is predicted by the stochastic growth theory. Higher amplitudes deviate from the lognormal distribution and follow a power law distribution with an exponent of -1.37 ± 0.01. It was shown that the amplitude distribution follows the lognormal distribution in the entire amplitude range for spatially limited regions. The estimated energy density ratio W for the largest amplitudes does not exceed 10^{-2}. This result suggests that modulational instability is not relevant in the Langmuir wave saturation. Similar to other planetary foreshocks, electrostatic decay processes can be also important for the stronger electrostatic waves inside Saturn's foreshock.

Before January 2005, Cassini made most of its measurements of Langmuir waves in regions further from the tangent point and deeper inside the foreshock that showed smooth variations without a significant peak of median amplitude. After January 2005, Cassini obtained more observations close to the upstream foreshock boundary in both MLT sectors, resulting in higher amplitude variations and higher median amplitudes with a significant peak. The dependence of the wave intensity on the depth inside the foreshock shows an onset of the Langmuir waves close to the upstream boundary (DIFF = 0) and slowly decreasing intensity with increasing depth into the downstream of the foreshock. The magnitude of the wavefield variations is the largest close to the upstream boundary and decreases with increasing DIFF. The position of the maximum amplitude has been observed to be slightly shifted into the foreshock (DIFF$\sim$1 R_S). However, the estimated uncertainty in the calculation of the DIFF coordinate is larger than the observed offset, and

therefore, this shift is not statistically significant. On the other hand our results are in agreement with previous observations in Earth's foreshock and show that the bow shock model of *Went et al.* [2011] is reliable. The dependence of wave intensity on the distance along the magnetic field shows an amplitude decrease of almost one order of magnitude up to the distance of 100 R_S. The combination of both foreshock coordinates shows that a median amplitude is higher for positions close to the tangent point and decreases with increasing distance into the foreshock (along both DIFF and DIST coordinates). Positions of Langmuir wave observations follow the expected shape of the foreshock region between the tangent field line and the bow shock as its boundaries.

Acknowledgments

Observations of the electric field experiment RWPS/WBR and the magnetic field instrument MAG on Cassini are available on http://ppi.pds.nasa.gov. We acknowledge the use of the list of Cassini magnetopause and bow shock crossings compiled by H.J. McAndrews, S.J. Kanani, and J.C. Cutler. We thank the team of M.E. Hill from Johns Hopkins University Applied Physics Lab for the list of the averaged solar wind speeds obtained by the CHEMS/MIMI instrument. Both lists are available on http://mapsview.engin.umich.edu. This work has been supported by NASA through contract 1415150 with the Jet Propulsion Laboratory. O.S. and J.S. acknowledge support by Czech Science Foundation through grants GACR205/10-2279 and P209/12/2394, respectively. O.S. thanks for additional support from grant LH14010.

Michael Balikhin thanks the reviewers for their assistance in evaluating this paper.

References

Achilleos, N., et al. (2006), Orientation, location, and velocity of Saturn's bow shock: Initial results from the Cassini spacecraft, *J. Geophys. Res.*, *111*, A03201, doi:10.1029/2005JA011297.

Anderson, R. R., T. E. Eastman, D. A. Gurnett, L. A. Frank, and G. K. Parks (1981), Plasma waves associated with energetic particles streaming into the solar wind from the Earth's bow shock, *J. Geophys. Res.*, *86*, 4493–4510, doi:10.1029/JA086iA06p04493.

Bale, S. D., D. Burgess, P. J. Kellogg, K. Goetz, and S. J. Monson (1997a), On the amplitude of intense Langmuir waves in the terrestrial electron foreshock, *J. Geophys. Res.*, *102*, 11,281–11,286, doi:10.1029/97JA00938.

Bale, S. D., G. Chisham, D. Burgess, and S. J. Schwartz (1997b), Langmuir wave amplitudes and the electron distribution function near the solar wind-foreshock boundary, *Adv. Space Res.*, *20*, 695–698, doi:10.1016/S0273-1177(97)00457-2.

Bale, S. D., D. E. Larson, R. P. Lin, P. J. Kellogg, K. Goetz, and S. J. Monson (2000), On the beam speed and wavenumber of intense electron plasma waves near the foreshock edge, *J. Geophys. Res.*, *105*, 27,353–27,368, doi:10.1029/2000JA900042.

Boshuizen, C. R., I. H. Cairns, and P. A. Robinson (2001), Stochastic growth theory of spatially-averaged distributions of Langmuir Fields in Earth's foreshock, *Geophys. Res. Lett.*, *28*, 3569–3572, doi:10.1029/2000GL012709.

Boshuizen, C. R., I. H. Cairns, and P. A. Robinson (2004), Electric field distributions for Langmuir waves in planetary foreshocks, *J. Geophys. Res.*, *109*, A08101, doi:10.1029/2004JA010408.

Cairns, I. H., and P. A. Robinson (1997), First test of stochastic growth theory for Langmuir waves in Earth's foreshock, *Geophys. Res. Lett.*, *24*, 369–372, doi:10.1029/97GL00084.

Cairns, I. H., P. A. Robinson, R. R. Anderson, and R. J. Strangeway (1997), Foreshock Langmuir waves for unusually constant solar wind conditions: Data and implications for foreshock structure, *J. Geophys. Res.*, *102*, 24,249–24,264, doi:10.1029/97JA02168.

Cairns, I. H., P. A. Robinson, and N. I. Smith (1998), Arguments against modulational instabilities of Langmuir waves in Earth's foreshock, *J. Geophys. Res.*, *103*, 287–300, doi:10.1029/97JA02871.

Dougherty, M. K., et al. (2004), The Cassini magnetic field investigation, *Space Sci. Rev.*, *114*, 331–383, doi:10.1007/s11214-004-1432-2.

Etcheto, J., and M. Faucheux (1984), Detailed study of electron plasma waves upstream of the Earth's bow shock, *J. Geophys. Res.*, *89*, 6631–6653, doi:10.1029/JA089iA08p06631.

Filbert, P. C., and P. J. Kellogg (1979), Electrostatic noise at the plasma frequency beyond the Earth's bow shock, *J. Geophys. Res.*, *84*, 1369–1381, doi:10.1029/JA084iA04p01369.

Fuselier, S. A., D. A. Gurnett, and R. J. Fitzenreiter (1985), The downshift of electron plasma oscillations in the electron foreshock region, *J. Geophys. Res.*, *90*, 3935–3946, doi:10.1029/JA090iA05p03935.

Greenstadt, E. (1976), Phenomenology of the Earth's bow shock system. A summary description of experimental results, in *Magnetospheric Particles and Fields, Astrophysics and Space Science Library*, vol. 58, edited by B. McCormac, pp. 13–28, Springer, Netherlands, doi:10.1007/978-94-010-1503-5_2.

Gurnett, D., et al. (2004), The Cassini radio and plasma wave investigation, *Space Sci. Rev.*, *114*(1-4), 395–463, doi:10.1007/s11214-004-1434-0.

Gurnett, D. A., and A. Bhattacharjee (2005), *Introduction to Plasma Physics*, Cambridge Univ. Press, Cambridge, U. K., and New York.

Gurnett, D. A., W. S. Kurth, and F. L. Scarf (1981), Plasma waves near Saturn—Initial results from Voyager 1, *Science*, *212*, 235–239, doi:10.1126/science.212.4491.235.

Gurnett, D. A., W. S. Kurth, F. L. Scarf, and R. L. Poynter (1986), First plasma wave observations of Uranus, *Science*, *233*, 106–109, doi:10.1126/science.233.4759.106.

Gurnett, D. A., et al. (1992), Plasma wave observations at Neptune, *Adv. Space Res.*, *12*, 47–54, doi:10.1016/0273-1177(92)90422-T.

Hospodarsky, G. B., D. A. Gurnett, W. S. Kurth, M. G. Kivelson, R. J. Strangeway, and S. J. Bolton (1994), Fine structure of Langmuir waves observed upstream of the bow shock at Venus, *J. Geophys. Res.*, *99*, 13,363–13,371, doi:10.1029/94JA00868.

Hospodarsky, G. B., W. S. Kurth, D. A. Gurnett, P. Zarka, P. Canu, M. K. Dougherty, G. H. Jones, A. Coate, and A. Rymer (2006), Observations of Langmuir waves detected by the Cassini spacecraft, in *Planetary Radio Emissions VI*, edited by H. O. Rucker, W. Kurth, and G. Mann, pp. 67, Aust. Acad. of Sci. Press, Vienna.

Jackman, C. M., R. J. Forsyth, and M. K. Dougherty (2008), The overall configuration of the interplanetary magnetic field upstream of Saturn as revealed by Cassini observations, *J. Geophys. Res.*, *113*, A08114, doi:10.1029/2008JA013083.

Krasnoselskikh, V. V., V. V. Lobzin, K. Musatenko, J. Soucek, J. S. Pickett, and I. H. Cairns (2007), Beam-plasma interaction in randomly inhomogeneous plasmas and statistical properties of small-amplitude Langmuir waves in the solar wind and electron foreshock, *J. Geophys. Res.*, *112*, A10109, doi:10.1029/2006JA012212.

Malaspina, D. M., B. Li, I. H. Cairns, P. A. Robinson, Z. Kuncic, and R. E. Ergun (2009), Terrestrial foreshock Langmuir waves: STEREO observations, theoretical modeling, and quasi-linear simulations, *J. Geophys. Res.*, *114*, A12101, doi:10.1029/2009JA014493.

Masters, A., N. Achilleos, M. K. Dougherty, J. A. Slavin, G. B. Hospodarsky, C. S. Arridge, and A. J. Coates (2008), An empirical model of Saturn's bow shock: Cassini observations of shock location and shape, *J. Geophys. Res.*, *113*, A10210, doi:10.1029/2008JA013276.

Musatenko, K., V. Lobzin, J. Soucek, V. V. Krasnoselskikh, and P. Décréau (2007), Statistical properties of small-amplitude Langmuir waves in the Earth's electron foreshock, *Planet. Space Sci.*, *55*, 2273–2280, doi:10.1016/j.pss.2007.05.025.

Press, W. H., S. A. Teukolsky, W. T. Vetterling, and B. P. Flannery (1992), *Numerical Recipes in C. The Art of Scientific Computing,* 2nd ed., Cambridge Univ. Press, Cambridge.

Robinson, P. A. (1992), Clumpy Langmuir waves in type III radio sources, *Sol. Phys.*, *139*, 147–163, doi:10.1007/BF00147886.

Robinson, P. A. (1995), Stochastic wave growth, *Phys. Plasmas*, *2*, 1466–1479, doi:10.1063/1.871362.

Robinson, P. A., and I. H. Cairns (1993), Stochastic growth theory of type III solar radio emission, *Astrophys. J.*, *418*, 506, doi:10.1086/173412.

Robinson, P. A., and I. H. Cairns (1995), Maximum Langmuir fields in planetary foreshocks determined from the electrostatic decay threshold, *Geophys. Res. Lett.*, *22*, 2657–2660, doi:10.1029/95GL01779.

Scarf, F. L., R. W. Fredricks, L. A. Frank, and M. Neugebauer (1971), Nonthermal electrons and high-frequency waves in the upstream solar wind: 1. Observations, *J. Geophys. Res.*, *76*, 5162–5171, doi:10.1029/JA076i022p05162.

Scarf, F. L., D. A. Gurnett, W. S. Kurth, and R. L. Poynter (1982), Voyager 2 plasma wave observations at Saturn, *Science*, *215*, 587–594, doi:10.1126/science.215.4532.587.

Sigsbee, K., C. Kletzing, D. Gurnett, J. Pickett, A. Balogh, and E. Lucek (2004a), Statistical behavior of foreshock Langmuir waves observed by the Cluster wideband data plasma wave receiver, *Ann. Geophys.*, *22*, 2337–2344, doi:10.5194/angeo-22-2337-2004.

Sigsbee, K., C. A. Kletzing, D. A. Gurnett, J. S. Pickett, A. Balogh, and E. Lucek (2004b), The dependence of Langmuir wave amplitudes on position in Earth's foreshock, *Geophys. Res. Lett.*, *31*, L07805, doi:10.1029/2004GL019413.

Sigsbee, K., C. A. Kletzing, J. S. Pickett, D. A. Gurnett, S. J. Schwartz, B. Lefebvre, E. Lucek, A. N. Fazakerley, and H. Kucharek (2010), Characteristics of Langmuir electric field waveforms and power spectra exhibiting nonlinear behavior in Earth's foreshock, *J. Geophys. Res.*, *115*, A10251, doi:10.1029/2009JA014948.

Soucek, J., V. Krasnoselskikh, T. Dudok de Wit, J. Pickett, and C. Kletzing (2005), Nonlinear decay of foreshock Langmuir waves in the presence of plasma inhomogeneities: Theory and Cluster observations, *J. Geophys. Res.*, *110*, A08102, doi:10.1029/2004JA010977.

Tsurutani, B. T., and R. G. Stone (1985), *Collisionless Shocks in the Heliosphere: Reviews of Current Research, Geophys. Monogr. Ser.*, vol. 35, AGU, Washington D. C.

Went, D. R., G. B. Hospodarsky, A. Masters, K. C. Hansen, and M. K. Dougherty (2011), A new semiempirical model of Saturn's bow shock based on propagated solar wind parameters, *J. Geophys. Res.*, *116*, A07202, doi:10.1029/2010JA016349.

Zimbardo, G., and P. Veltri (1996), Spreading and intermittent structure of the upstream boundary of planetary magnetic foreshocks, *Geophys. Res. Lett.*, *23*, 793–796, doi:10.1029/96GL00660.